



Hot deformation behaviors and dynamic recrystallization mechanism of Ti-35421 alloy in β single field

Tong LU^{1,2}, Zhen-hua DAN¹, Kai LI³, Dan-qing YI⁴, Lian ZHOU¹, Hui CHANG¹

1. College of Materials Science and Engineering and Tech Institute for Advanced Materials, Nanjing Tech University, Nanjing 210009, China;
2. Suzhou Branch, Chinalco Materials Application Research Institute Co., Ltd., Suzhou 215026, China;
3. Chinalco Materials Application Research Institute Co., Ltd., Beijing 102209, China;
4. School of Materials Science and Engineering, Central South University, Changsha 410083, China

Received 13 August 2021; accepted 29 December 2021

Abstract: Hot deformation behaviors and microstructure evolution of Ti-3Al-5Mo-4Cr-2Zr-1Fe (Ti-35421) alloy in the β single field are investigated by isothermal compression tests on a Gleeble-3500 simulator at temperatures of 820–900 °C and strain rates of 0.001–1 s⁻¹. The research results show that discontinuous yield phenomenon and rheological softening are affected by the strain rates and deformation temperatures. The critical conditions for dynamic recrystallization and kinetic model of Ti-35421 alloy are determined, and the Arrhenius constitutive model is constructed. The rheological behaviors of Ti-35421 alloys above β phase transformation temperature are predicted by the constitutive model accurately. The EBSD analysis proves that the deformation softening is controlled by dynamic recovery and dynamic recrystallization. In addition, continuous dynamic recrystallization is determined during hot deformation, and the calculation model for recrystallization grain sizes is established. Good linear dependency between the experimental and simulated values of recrystallized grain sizes indicates that the present model can be used for the prediction of recrystallized grain size with high accuracy.

Key words: Ti-3Al-5Mo-4Cr-2Zr-1Fe alloy; microstructure evolution; Arrhenius constitutive model; deformation softening; continuous dynamic recrystallization

1 Introduction

Owing to the high yield strength, excellent resistance to fatigue crack growth and corrosion, titanium and its alloys have been widely used in many key fields [1–3]. The near- β titanium alloys have some advantages compared with other commercial titanium alloys, including complete β phases after quenching, lower β transformation temperature (T_β), good welding performance, superior combination of strength, plasticity and excellent processing performance [4–6]. Due to these merits, the near- β titanium alloys have

been used for the manufacture of the parts of airplanes, automobiles, and human-occupied vehicles [7]. However, many near- β alloys, such as Ti-5Al-5Mo-5V-1Cr-1Fe (Ti-55511), Ti-5Al-5Mo-5V-3Cr-1Zr (Ti-55531), Ti-5Al-5Mo-5V-3Cr (Ti-5553) and Ti-10V-2Fe-3Al (Ti-1023) [8–11] contain high-value alloying elements, typical V element, which weaken the cost advantages and limit their large-scale application. Hence, the strategy of the replacements of high-price V element by low-price elements for the improvement of the mechanical performance becomes attractive for near- β titanium alloys. Ti-3Al-5Mo-4Cr-2Zr-1Fe (Ti-35421) alloy was a

new low-cost near- β titanium alloy based on Ti-3Al-5Mo-5V-4Cr-2Zr (Ti-B19) [12]. The Ti-35421 alloy was obtained by replacing the V element in Ti-B19 alloy with low-cost Fe element and keeping the Mo equivalent constant, and it has the strength of 900–1450 MPa and elongation of 6%–15% [13].

As has been known, work hardening (WH), dynamic recovery (DRV) and dynamic recrystallization (DRX) occur in titanium alloys with low stacking faults during thermal deformation [14–17]. These phenomena complicate the hot deformation process and affect the evolution of the microstructure and mechanical properties. In addition, the hot deformation parameters, including deformation temperature, strain rate and strain, are the main factors leading to changes in the deformation behaviors of titanium alloys [18–20]. In order to design and optimize the hot deformation parameters of low-cost Fe-containing titanium alloys, and provide the theoretical basis for industrial production, the hot deformation of Ti-35421 alloy is deserved to be investigated in detail. It is of great significance to study the influence of microstructure evolution on flow behaviors and discuss the mechanism of the hot deformation.

Over the last few years, a large number of helpful studies have been conducted on the hot deformation behaviors in compression mode and microstructure evolution of Fe-containing near- β titanium alloys. LIANG et al [21] investigated the dynamic recrystallization behaviors of Ti-55511 alloy and obtained the dependence of DRX process on deformation parameters from Avrami kinetics analysis. BALASUBRAHMANYAM and PRASAD [22] analyzed the hot deformation behaviors of Ti-10V-4.5Fe-1.5Al alloy and found that DRX occurred in the temperature range of 750–900 °C and strain rate range of 0.001–0.1 s⁻¹. WANG et al [23] investigated the precipitation behaviors of Ti-55511 alloy during hot compression and found that the deformation mechanism was related to deformation parameters. The above research is very useful for understanding the deformation mechanism and microstructure evolution of Fe-containing near- β titanium alloy above T_β . However, there are few studies on the constitutive models of the hot deformation and microstructure evolution of Fe-containing low-cost titanium alloys. At the same time, the effects of

DRV and DRX on the flow stresses and DRX mechanism in the single-phase region are not clear. Therefore, it is necessary to construct the constitutive models and understand the hot deformation mechanisms in order to guide the hot deformation process of near- β titanium alloys above T_β .

In this study, the hot deformation behaviors and DRV, DRX and continuous dynamic recrystallization (CDRX) mechanisms of Ti-35421 titanium alloy above T_β are investigated. A newly-developed constitutive model with better accuracy is aimed to establish for the analysis of WH, DRV and DRX based on the hot compression experiments and further to use to predict the flow stresses during the hot deformation. The critical conditions for the occurrence of DRX are extracted and the DRX kinetic model is built up. The depending relationship between the predicted value based on the constitutive model and the experimental data is investigated. Furthermore, the influence of hot deformation parameters on the microstructure evolution of the Ti-35421 titanium alloy is analyzed by EBSD. The deformation softening mechanism is discussed. It is highly expected that the recrystallized grain size can be predicted by the present model more accurately.

2 Experimental

The Ti-35421 alloy with compositions of 3.04Al-5.14Mo-4.22Cr-2.08Zr-0.99Fe-Ti (wt.%) was used in this study and T_β of Ti-35421 was determined to be (803±5) °C by the metallographic method. The as-received Ti-35421 slabs were held at 860 °C for 0.5 h followed by air cooling to obtain a single phase β microstructure. Hot deformation behaviors were investigated by the hot deformation tests on a Gleeble-3500 mechanical simulator. The schematic experimental process of the Ti-35421 alloy is shown in Fig. 1. The compressed samples had dimensions of 12 mm in height and 8 mm in diameter. The deformation temperatures were set to be 820, 840, 860, and 900 °C, respectively. The samples were heated to the setting temperature with a heating rate of 10 °C/s and homogenized for 0.5 h. The specimens were immediately quenched by water to reserve the deformed microstructure. The specimen was compressed at the strain rates of 0.001–1 s⁻¹ and a height reduction of 60%. The

slices parallel to the compression axis direction at the center position of the compressed samples were selected for the microstructural analysis. For the electron backscatter diffraction (EBSD) examination, the specimens were electro-polished in a solution of 95% acetic acid and 5% perchloric acid at 25 °C with the voltage of 35 V and the polishing time of 40 s. The scanned area was 500 $\mu\text{m} \times 400 \mu\text{m}$ and the step size was 0.5 μm . The data were analyzed using the OIM Analysis software. The boundaries with misorientations between 2° and 15° were defined as low-angle grain boundaries (LAGBs), while those with misorientations larger than 15° were defined as high-angle grain boundaries (HAGBs). White and black lines in EBSD maps indicate LAGBs and HAGBs, respectively.

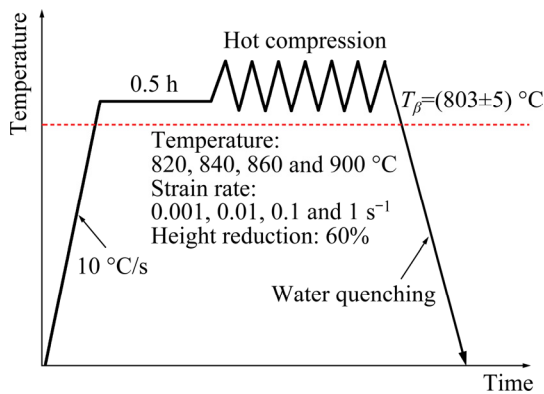


Fig. 1 Schematic experimental process of Ti-35421 alloy

3 Results

3.1 Hot deformation behaviors of Ti-35421 alloys above T_{β}

The initial microstructure of the Ti-35421 alloy solution treated at 860 °C for 0.5 h is shown in Fig. 2(a). The starting material after solution treatment comprised equiaxed β grains with the average size of about 200 μm . Different colors represent different grain orientations and the colors of grain boundary represent different kinds of grain boundaries (LAGBs and HAGBs). The frequency of the LAGBs is 17.1% while that of the HAGBs is 82.9%. As shown in Fig. 2(b), several diffraction peaks centered at 2θ values of 39.05°, 56.28°, 70.19° and 82.95° are well assigned to (110), (200), (211) and (220) to β phases and one peak at 2θ value of 35.09° is arisen from α phase according to JCPDF Nos. 51-0631 and 44-1294, respectively. It

should be pointed out from the XRD pattern that the microstructure is almost full β phase with BCC structure in the quenched specimen.

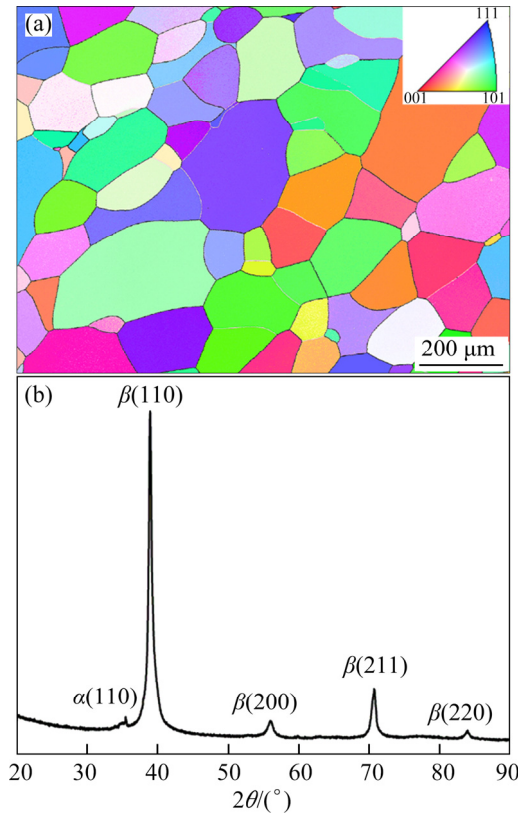


Fig. 2 Initial microstructure (a) and XRD pattern (b) of Ti-35421 alloy solution treated at 860 °C for 0.5 h

Figure 3 shows the typical true stress–strain curves, yield drop value ($\Delta\sigma$, $\Delta\sigma = \sigma_u - \sigma_l$, σ_u is the upper yield stress, and σ_l is the lower yield stress) and Y_d ($Y_d = \Delta\sigma / \sigma_u$) of Ti-35421 alloy at different temperatures (820, 840, 860 and 900 °C) and strain rates (0.001, 0.01, 0.1 and 1 s^{-1}). The true stress–strain curves have a similar tendency under different conditions. All curves have a single peak during the deformation process, which is consistent with the reported data [24]. Simultaneously, WH and dynamic softening also appear during the hot deformation. In this work, the discontinuous yield is quantified by the yield drop value and value of Y_d as shown in Figs. 3(e) and (f), respectively. It can be clearly seen from Fig. 3(e) that $\Delta\sigma$ gradually increases as the temperature decreases. At the same temperature, $\Delta\sigma$ increases firstly and then decreases when the strain rate increases. When the strain rate is high (0.1 s^{-1}), the yield drop value is also high, which is consistent with the reported case [25]. The $\Delta\sigma$ is related to chemical composition, grain size

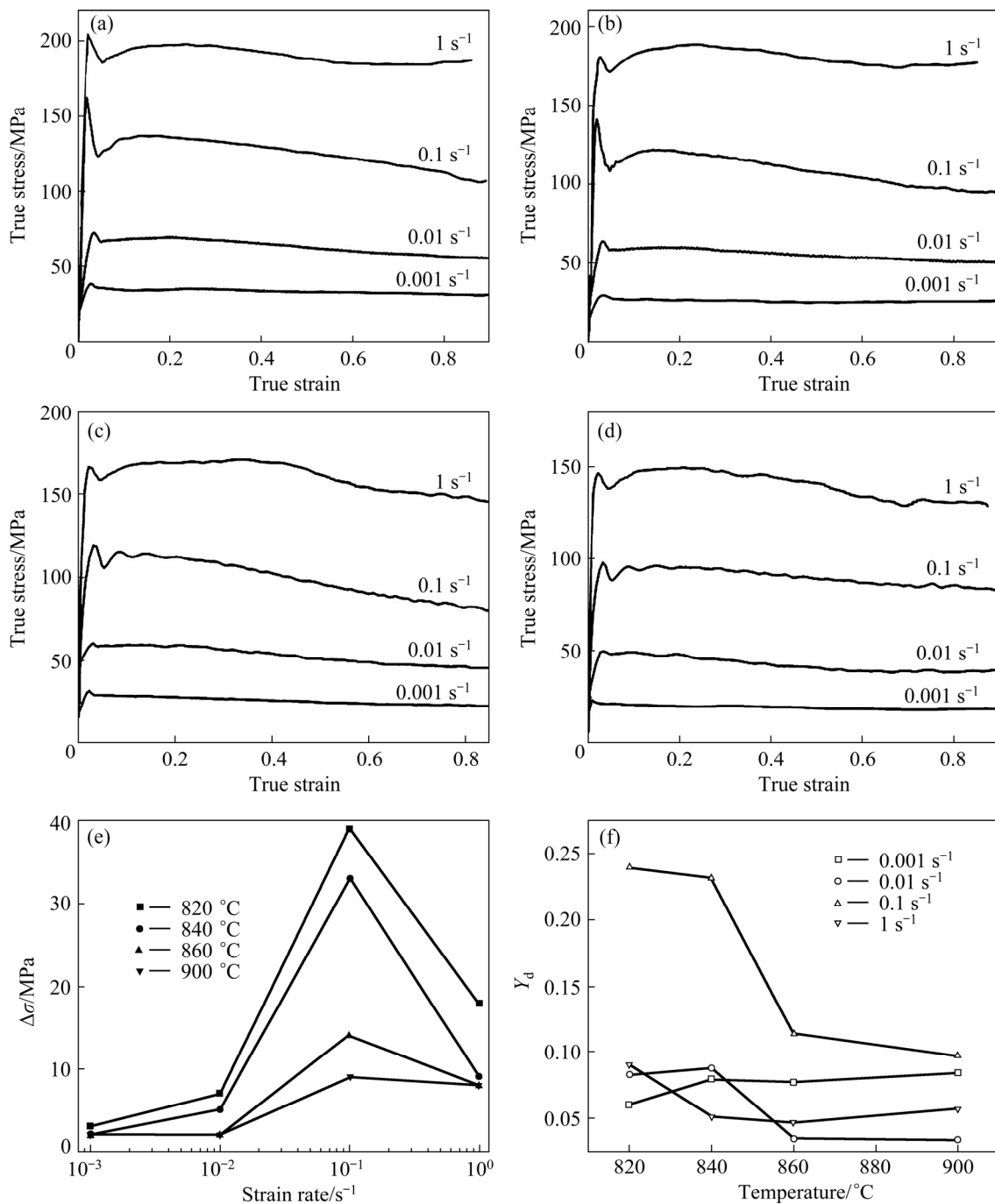


Fig. 3 True stress–true strain curves (a–d), yield drop value $\Delta\sigma$ (e) and value of Y_d (f) of Ti-35421 alloy under different conditions: (a) 820 °C; (b) 840 °C; (c) 860 °C; (d) 900 °C

and deformation parameters. For titanium alloys with different compositions, the type and content of β -stabilizing elements also affect the yield drop [26]. The value of Y_d exhibits a minimum at 820 °C and low strain rate (0.001 s⁻¹), as shown in Fig. 3(f). And it can be seen that the value of Y_d increases with the increase of strain rate. It is similar to the result of PHILIPPART and RACK [27]. The flow stress increases sharply and then reach its peak, and

at last it drops. This is known as the discontinuous yield phenomenon (DYP), and it is a distinctive feature when the hot compression temperature is above T_β . This has been observed in many near- β titanium alloys, such as Ti-10V-4.5Fe-1.5Al [22], Ti-55531 [28], and Ti-1023 [25]. FAN et al [29] has reported that mobile dislocations are generated at the grain boundaries and then diffuse into grain interior as the strain increases during the hot

deformation of the near- β titanium alloy.

In order to study the microstructure evolution of the Ti-35421 alloy deformed above T_β , the orientation maps of the samples at different deformation temperatures of 820–900 °C and strain rates of 0.001–1 s⁻¹ were analyzed. Figure 4 shows the effect of the strain rate on the evolution of microstructure. When the strain rate is 0.001 s⁻¹, the equiaxed subgrains are formed within the grains and the size is similar to the recrystallized grain size (Figs. 4(m) and (p)). As the strain rate increases, the substructures begin to become discontinuous, and they are mainly distributed near the pre-existing boundaries of β grains. In addition, the size of substructure decreases with the increase of the strain rates, which is ascribed to insufficient time for the dislocations to slide and climb at the high strain rates. Simultaneously, the recrystallized grains also change significantly as the deformation rate increases. The approximately equiaxed recrystallized grains are obtained at 0.001 s⁻¹. When

the strain rate increases to 0.01 s⁻¹ in Figs. 4(i–l), the size of DRX grains becomes smaller and the number of subgrains decreases. As the strain rate further increases to 1 s⁻¹, smaller DRX grains are formed along the original HAGBs and DRX grains are smaller due to the short deformation time, as shown in Figs. 4(a–d). The effect of temperature on the evolution of microstructure can be revealed in Fig. 4. As the temperature increases, the volume fraction and grain size of recrystallized grains increase significantly, especially at lower strain rates (≤ 0.01 s⁻¹). In addition, a large number of LAGBs (white lines) can be found at lower temperatures (Fig. 4(m)). As the temperature increases, the LAGBs gradually decrease. This is considered that the LAGBs absorb dislocations to result in the formation of HAGBs and form HAGBs-recrystallized grains at higher temperatures. At the same time, when the strain rate is low (≤ 0.01 s⁻¹), the recrystallized grains have sufficient time to grow up. Thus, the volume fraction and size

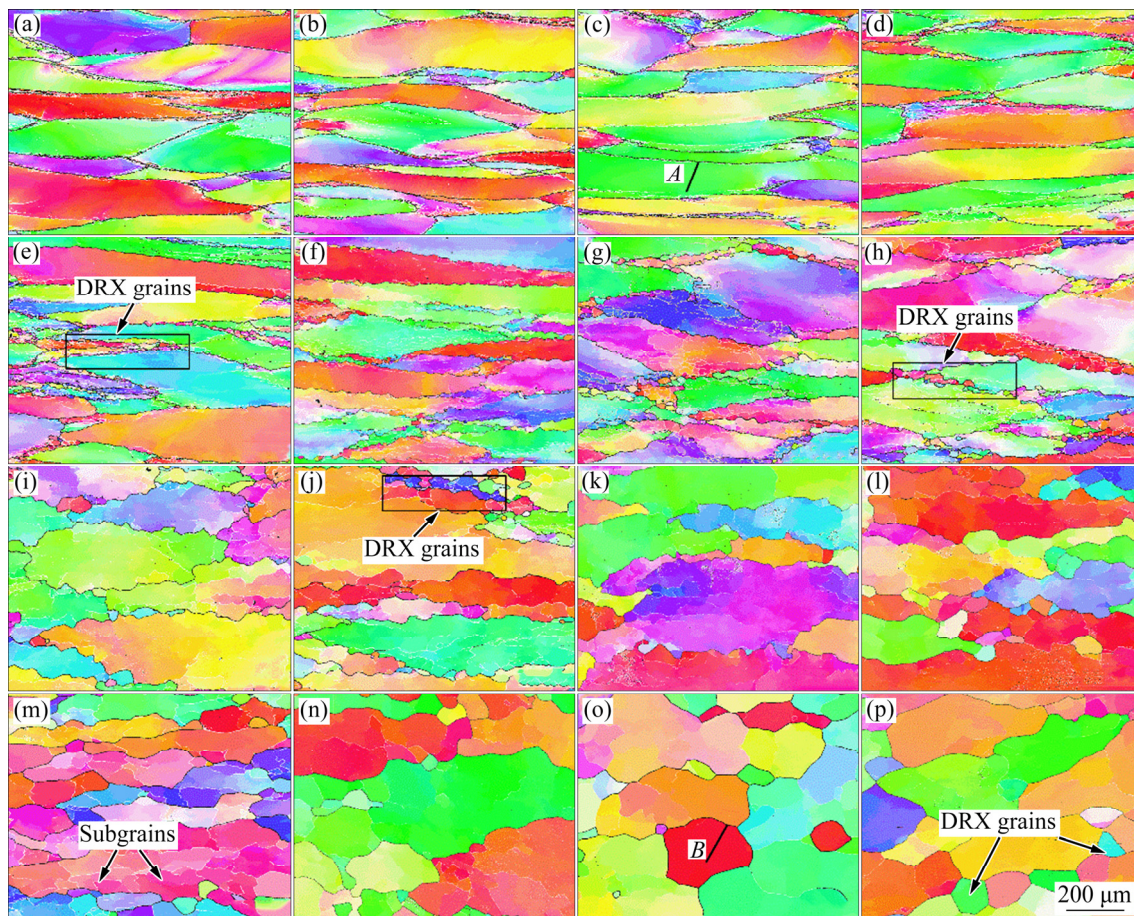


Fig. 4 Orientation maps of deformed samples at different temperatures and strain rates: (a) 820 °C, 1 s⁻¹; (b) 840 °C, 1 s⁻¹; (c) 860 °C, 1 s⁻¹; (d) 900 °C, 1 s⁻¹; (e) 820 °C, 0.1 s⁻¹; (f) 840 °C, 0.1 s⁻¹; (g) 860 °C, 0.1 s⁻¹; (h) 900 °C, 0.1 s⁻¹; (i) 820 °C, 0.01 s⁻¹; (j) 840 °C, 0.01 s⁻¹; (k) 860 °C, 0.01 s⁻¹; (l) 900 °C, 0.01 s⁻¹; (m) 820 °C, 0.001 s⁻¹; (n) 840 °C, 0.001 s⁻¹; (o) 860 °C, 0.001 s⁻¹; (p) 900 °C, 0.001 s⁻¹

of the recrystallized grains are significantly increased.

3.2 Constitutive model coupled with DRX

As we all known, the diffusion activation energy is an important indicator to determine the deformation mechanism. If the activation energy is similar to the self-diffusion activation energy of pure β titanium alloy, it indicates that the main deformation mechanism is DRV [30]. In this work, the peak stress was selected to calculate activation energy. For the metallic materials, the Zener–Hollomon parameter (Z) can be described as follows [31,32]:

$$\ln Z = \ln \dot{\epsilon} + \frac{Q}{RT} = \ln A + n \ln[\sinh(\alpha\sigma)] \quad (1)$$

$$\ln \dot{\epsilon} = \begin{cases} \ln B + n_1 \ln \sigma - Q/(RT) & (\alpha\sigma < 0.8) \\ \ln C + \beta\sigma - Q/(RT) & (\alpha\sigma > 1.2) \end{cases} \quad (2)$$

where $\dot{\epsilon}$ is the strain rate; Q is the activation energy; T is the absolute temperature (K); R is the molar gas constant (8.314 J/(mol·K)); A , B , C , n_1 and β are the material constants; σ is the stress; n is the stress component; $\alpha = \beta/n_1$. Equation (3) can be

obtained by taking the partial derivatives with respect to T of Eq. (1):

$$Q = R \left[\frac{\partial \ln \dot{\epsilon}}{\partial \ln[\sinh(\alpha\sigma)]} \right]_T \left[\frac{\partial \ln[\sinh(\alpha\sigma)]}{\partial (1/T)} \right]_{\dot{\epsilon}} \quad (3)$$

In order to predict the flow stress more accurately, the effect of strain on the material constants should be considered [9]. According to Eq. (2) and Eq. (3), the values of n_1 and β are determined by calculating the slope of the curve, as shown in Figs. 5(a) and (b). The value of α can be determined by the values of n_1 and β ($\alpha = \beta/n_1 = 0.01274$). The reciprocal of the average slope in Fig. 5(c) is 2.831, and the average slope in Fig. 5(d) is 9.707. Based on the data and molar gas constant (R), the value of activation energy is determined to be 228.5 kJ/mol (Eq. (3)). The self-diffusion activation energy of pure β titanium alloy is 153 kJ/mol [30]. DRV and DRX occur at higher temperatures. The value of Q is higher than 153 kJ/mol, which indicates that DRV and DRX occur simultaneously. Therefore, the corresponding true stress–true strain curves of Ti-35421 alloy can be divided into two types, as shown in Fig. 6 [33].

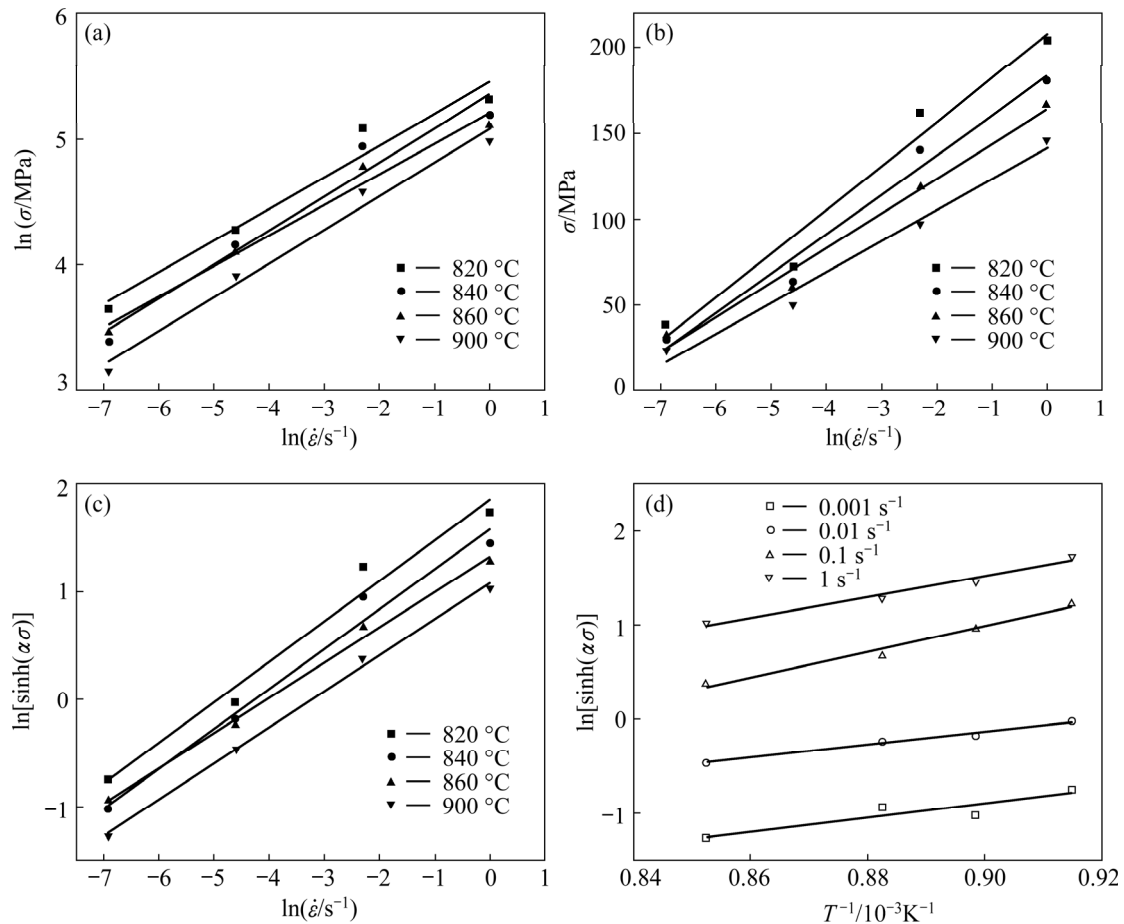


Fig. 5 Relationships of $\ln \sigma - \ln \dot{\epsilon}$ (a), $\sigma - \ln \dot{\epsilon}$ (b), $\ln[\sinh(\alpha\sigma)] - \ln \dot{\epsilon}$ (c), and $\ln[\sinh(\alpha\sigma)] - 1/T$ (d)

The true stress–strain curves during DRV can be illustrated by Line *a* in Fig. 6 [33]. First of all, the stress increases quickly and WH begins to appear; afterward, the gradual decrease of the slope indicates that the material begins to deform uniformly and WH undergoes. With the strengthening of WH, DRV begins to appear and gradually strengthens. The softening caused by DRV gradually offsets the WH effect, and the slope of the curve decreases and tends to be horizontal. Finally, the WH caused by deformation and the softening caused by DRV are balanced, the flow stress stops increasing and becomes saturated (σ_{sat}), and the true stress–strain curve remains horizontal. The true stress–strain curve during DRX can be explained by Line *b* in Fig. 6. It can be divided into three stages. In Stage I, the stress rises rapidly with the increase of strain due to the WH. In Stage II, the strain reaches the critical value ε_c , the DRX begins and its softening effect gradually increases with increasing strain. When $\sigma > \sigma_p$ (σ_p is the peak stress), the softening effect of DRX exceeds WH and the stress decreases with increasing strain. In Stage III, the WH and the softening caused by DRX tend to balance as the strain increases, the flow stress tends to become steady (σ_{ss}). In order to establish the model describing the relationship among WH, DRV and DRX, the parameters in Fig. 6 need to be determined, including the yield stress (σ_0), saturated stress (σ_{sat}), steady stress (σ_{ss}), critical strain (ε_c), and peak strain (ε_p).

Based on the dislocation density theory, the evolution of dislocation density mainly includes the multiplication and annihilation of dislocations. The flow stress during DRV and WH (σ_{rec}) can be expressed as

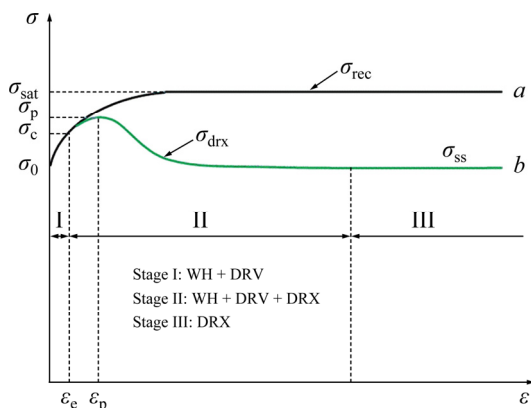


Fig. 6 Stress–strain curves including WH, DRV and DRX [33]

$$\sigma_{\text{rec}} = \sqrt{\sigma_{\text{sat}}^2 + (\sigma_0^2 - \sigma_{\text{sat}}^2) \cdot \exp(-\Omega\varepsilon)} \quad (\varepsilon < \varepsilon_c) \quad (4)$$

where ε is the strain, and Ω is the coefficient of DRV.

It can be seen from Eq. (4) that the three parameters (σ_{sat} , σ_0 and Ω) need to be determined in order to get the value of σ_{rec} . Generally, the Zener–Hollomon parameter can be used to characterize the influence of different hot deformation conditions on the characteristic parameters of stress–strain curves (such as σ_{sat} , σ_0 and Ω). The value of yield stress (σ_0) at different temperatures and strain rates can be acquired from the stress–strain curves. The yield stress (σ_0) is taken as the stress corresponding to an offset strain of 0.02. A third order polynomial is used to fit the relationship between σ_0 and $\ln Z$, which can be written as Eq. (5). Figure 7(a) shows that the experimental data and the fitted curves have a good correlation.

$$\sigma_0 = -0.32(\ln Z)^3 + 21.79(\ln Z)^2 - 459.52 \ln Z + 3135 \quad (5)$$

Figure 7(b) shows that a third order polynomial is established to model the relationship between the saturated stress (σ_{sat}) and $\ln Z$. The equation can be expressed as

$$\sigma_{\text{sat}} = -0.35(\ln Z)^3 + 23.23(\ln Z)^2 - 479.62 \ln Z + 3219 \quad (6)$$

DRV is the main softening mechanism when the strain is less than the critical strain of DRX during hot deformation process. Therefore, the value of Ω can be calculated using the stage before the critical strain in the stress–strain curve. Figure 7(c) shows that there is a linear relationship between the $\ln \Omega$ and $\ln Z$, and the relationship between Ω and Z can be expressed as

$$\Omega = \exp(0.27 \ln Z - 1.66) \quad (7)$$

Therefore, the constitutive relation of the Ti-35421 alloy during the WH and DRV can be expressed as

$$\begin{cases} \sigma_{\text{rec}} = \sqrt{\sigma_{\text{sat}}^2 + (\sigma_0^2 - \sigma_{\text{sat}}^2) \cdot \exp(-\Omega\varepsilon)} \\ \sigma_0 = -0.32(\ln Z)^3 + 21.79(\ln Z)^2 - 459.52 \ln Z + 3135 \\ \sigma_{\text{sat}} = -0.35(\ln Z)^3 + 23.23(\ln Z)^2 - 479.62 \ln Z + 3219 \quad (\varepsilon < \varepsilon_c) \\ \Omega = \exp(0.27 \ln Z - 1.66) \\ Z = \dot{\varepsilon} \exp\left(-\frac{228500}{RT}\right) \end{cases} \quad (8)$$

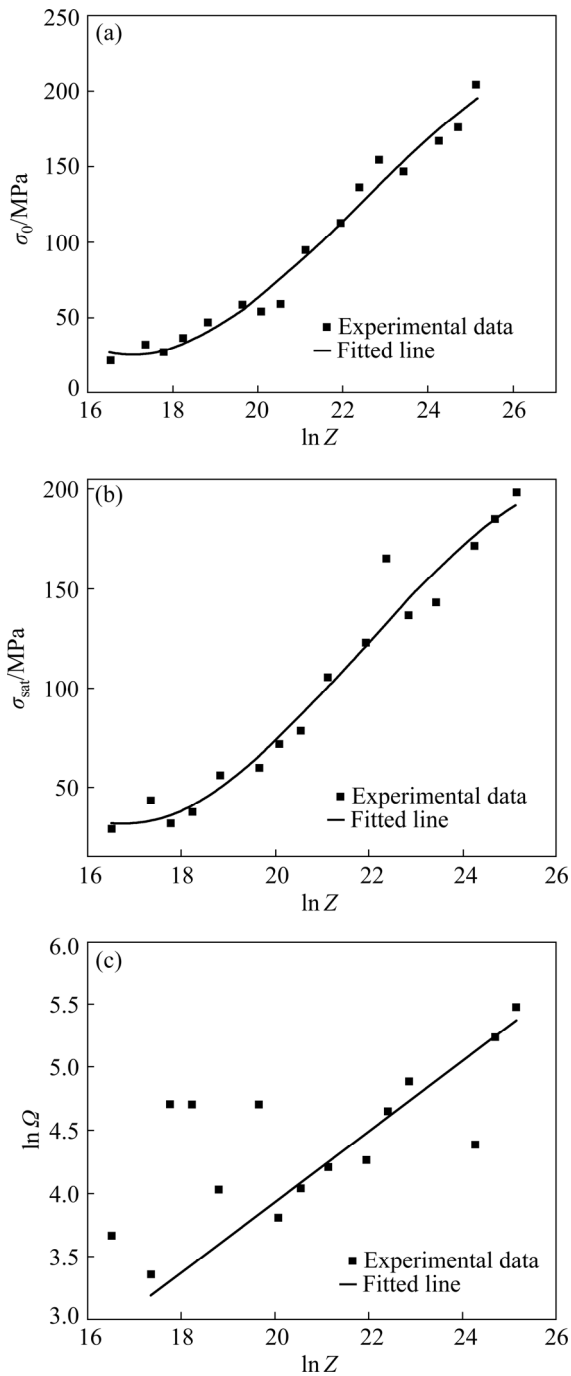


Fig. 7 Relationships between σ_0 and $\ln Z$ (a), σ_{sat} and $\ln Z$ (b), and $\ln Q$ and $\ln Z$ (c)

Equation (8) can be used to predict the flow stresses of the Ti-35421 alloy during the hot deformation stage with the temperatures and strain rates of 820 to 900 °C and 0.001 to 1 s⁻¹, respectively. By analyzing the stress–strain curves and the results of the EBSD data, it can be concluded that DRX occurs in the Ti-35421 alloy. However, the moment when DRX happens cannot be intuitively obtained from the stress–strain curves and EBSD data. Therefore, it is necessary to

perform data processing on the stress–strain curves to obtain the θ – σ curves ($\theta=d\sigma/d\varepsilon$) and the $-d\theta/d\sigma$ curves, and then the critical point of the WH rate is used to determine ε_c and σ_p of DRX. When the critical condition of Ti-35421 recrystallization is determined by calculating the WH rate ($\theta=d\sigma/d\varepsilon$), the slope of the stress–strain curve corresponding to each strain can be obtained. Many researchers have proposed different mathematical models to determine the critical strains. WU and HUANG [33] determined the critical value by fitting a third-order polynomial. GOTTSTEIN et al [34] have determined the critical strain through the dislocation WH model. Combined with the principle of the incremental work balance in the thermodynamic system, POLIAK and JONAS [35] have proved that the critical condition for DRX is $d(-d\theta/d\sigma)/d\sigma=0$, which is the inflection point of the θ – σ curve or the lowest point of the $-(d\theta/d\sigma)$ – σ curve. This model has been employed to confirm the critical conditions here. Figure 8 shows the curves of θ – σ and $-(d\theta/d\sigma)$ – σ at 840 °C and 0.01 s⁻¹. The critical

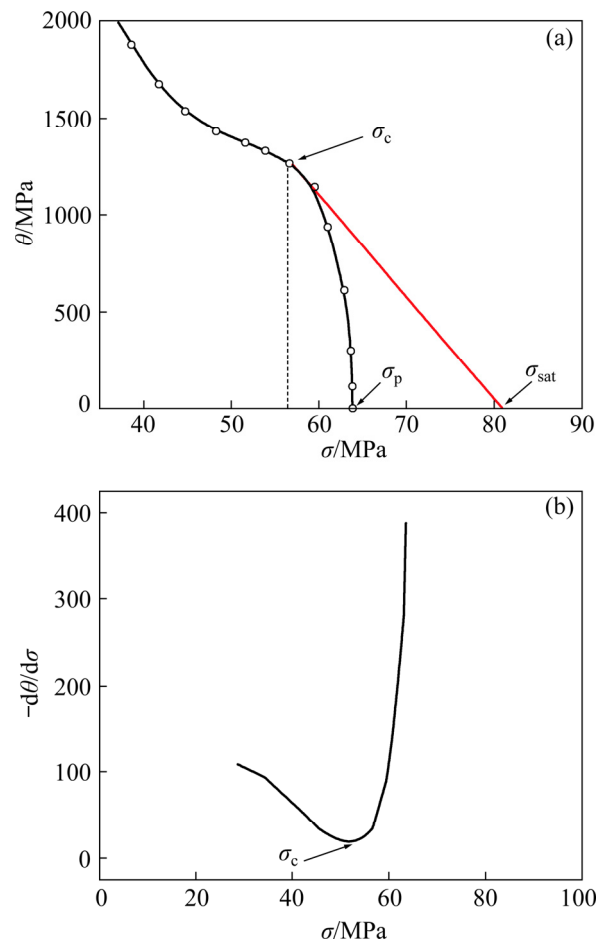


Fig. 8 Curves of θ – σ (a) and $-(d\theta/d\sigma)$ – σ (b) at 840 °C and 0.01 s⁻¹

stress (σ_c) for recrystallization is determined by the $-(d\theta/d\sigma)-\sigma$ curve (Fig. 8(b)) and the peak stress (σ_p) is determined by the intersection of the curve and $\theta=0$ (Fig. 8(a)). The saturated stress (σ_{sat}) for DRV can be obtained by making the tangent line of σ_c and extrapolating the line to $\theta=0$ (Fig. 8(a)). After determining σ_c and σ_p , the corresponding ε_c and ε_p can be obtained from the stress–strain curves. The values of σ_c and ε_c under different hot deformation conditions are shown in Table 1. It can be concluded that the values of σ_c and ε_c are mainly affected by the strain rate and deformation temperature. As the strain rate increases, σ_c gradually increases. Figure 9 shows the $-(d\theta/d\sigma)-\sigma$ curves of Ti-35421 alloy under different hot deformation conditions. Obviously, each curve has a lowest point, which proves that DRX occurs under different conditions.

The analysis of DRX process and the calculation of volume fraction of recrystallized grains (X_{drx}) have attracted the interest of many researchers, where the kinetic model is commonly known. The kinetic model can be expressed as [36]

Table 1 Critical parameters σ_c and ε_c of DRX under different hot deformation conditions

Deformation temperature/°C	Strain rate/s ⁻¹	σ_c /MPa	ε_c
820	0.001	36.3	0.022
	0.01	67.6	0.020
	0.1	136.4	0.013
	1	196.7	0.020
840	0.001	27.1	0.020
	0.01	56.3	0.018
	0.1	121.2	0.012
	1	159.9	0.012
860	0.001	27.8	0.013
	0.01	59.3	0.026
	0.1	111.6	0.023
	1	163.4	0.042
900	0.001	22.3	0.013
	0.01	46.5	0.020
	0.1	93.5	0.024
	1	129.7	0.008

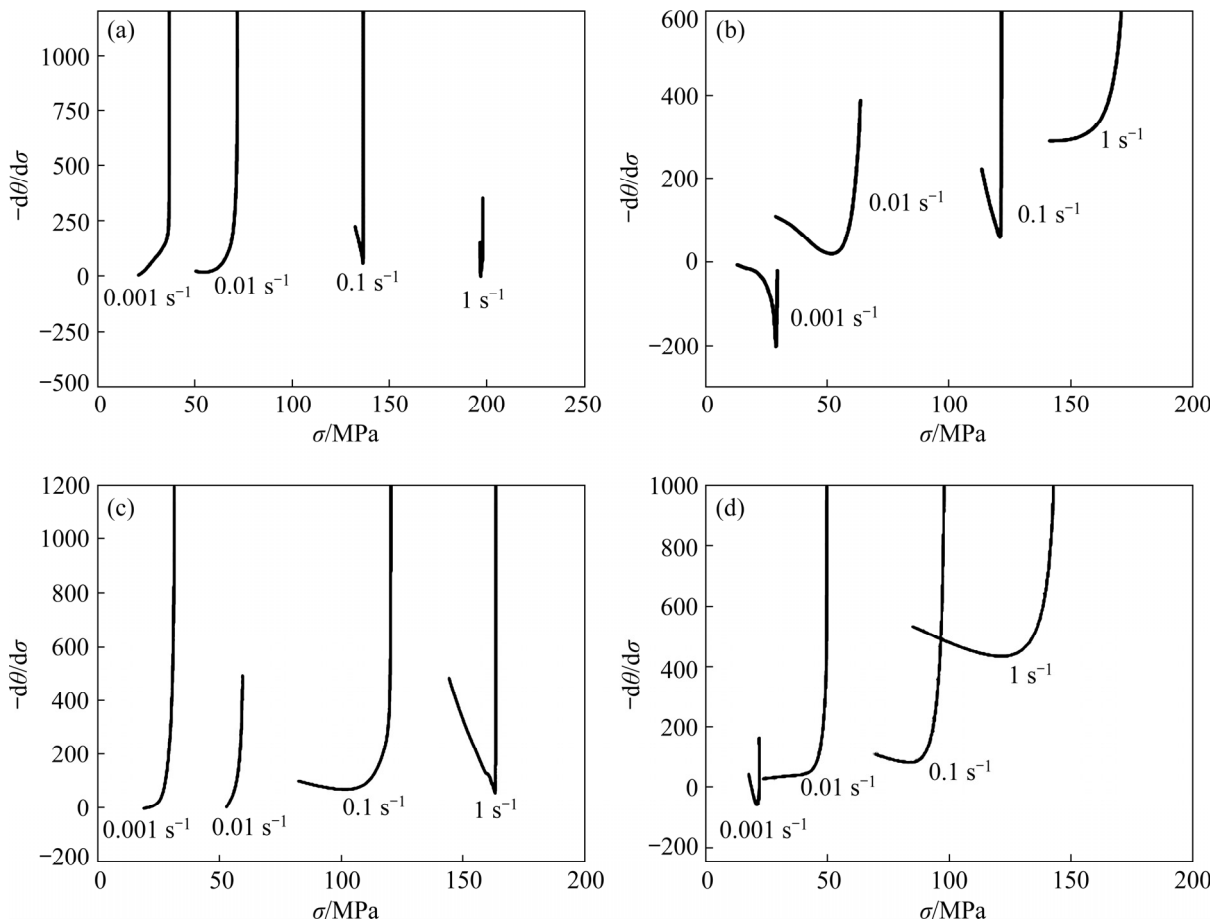


Fig. 9 Fitting curves of $-(d\theta/d\sigma)-\sigma$ at different temperatures: (a) 820 °C; (b) 840 °C; (c) 860 °C; (d) 900 °C

$$X_{\text{drx}} = 1 - \exp \left[-B \left(\frac{\varepsilon - \varepsilon_c}{\varepsilon_p} \right)^K \right] \quad (\varepsilon > \varepsilon_c) \quad (9)$$

where B and K are the material constants. Simultaneously, another formula can be used to calculate X_{drx} , which can be expressed as

$$X_{\text{drx}} = \frac{\Delta\sigma}{\sigma_{\text{sat}} - \sigma_{\text{ss}}} \quad (\varepsilon > \varepsilon_c) \quad (10)$$

where $\Delta\sigma$ is the difference between σ_{rec} and σ_{drx} , and it represents the net softening value caused by DRX.

A third order polynomial is adopted to fitting the relationship between σ_{ss} and $\ln Z$, and it can be represented as

$$\sigma_{\text{ss}} = 0.080(\ln Z)^3 - 3.09(\ln Z)^2 + 41.54\ln Z - 125.3 \quad (11)$$

Figure 10(a) shows that the third-order polynomial can predict the value of σ_{ss} more accurately.

In order to determine the DRX kinetic model of Ti-35421 alloy, the relationship between $\ln[-\ln(1-X_{\text{drx}})]$ and $\ln[(\varepsilon - \varepsilon_c)/\varepsilon_p]$ is shown in Fig. 10(b). The parameters B and K are obtained from the intercept and slope of the fitted curve as 0.0101 and 1.72, respectively. Therefore, the kinetic model expression of DRX is determined as

$$X_{\text{drx}} = 1 - \exp \left[-0.0101 \left(\frac{\varepsilon - \varepsilon_c}{\varepsilon_p} \right)^{1.72} \right] \quad (\varepsilon > \varepsilon_c) \quad (12)$$

The flow stress during the DRX can be obtained by substituting Eq. (12) into Eq. (10), and can be expressed as

$$\sigma_{\text{drx}} = \sigma_{\text{rec}} - (\sigma_{\text{sat}} - \sigma_{\text{ss}}) \cdot \left\{ 1 - \exp \left[-0.0101 \left(\frac{\varepsilon - \varepsilon_c}{\varepsilon_p} \right)^{1.72} \right] \right\} \quad (\varepsilon > \varepsilon_c) \quad (13)$$

Equations (8) and (13) are used to predict the flow stress of Ti-35421 alloy under different hot deformation conditions. Figure 11 shows the comparison between the predicted value of flow stress and the experimental data under different hot deformation conditions. The comparison shows that the predicted value is in good agreement with the experimental data at the strain softening stage. When the strain is less than 0.1, it is observed that there exist some errors, which is consistent with the reported results [15,37]. The reason for this may be that when the strain is less than 0.1, the stress change is affected by WH, DRV and DRX, and it is difficult to ensure that simulation calculations predict experimental measurements accurately. After the high-temperature constitutive equations are established based on different types of constitutive models, it is necessary to verify the accuracy of these equations to determine whether they can be used to predict flow stress in the actual processing of alloys.

Therefore, two standard statistical parameters in mathematics are used to describe the error distribution, namely the correlation coefficient (\bar{R}) and the average absolute relative error (AARE). They can be expressed as follows:

$$\bar{R} = \frac{\sum_{i=1}^N (E_i - \bar{E})(P_i - \bar{P})}{\sqrt{\sum_{i=1}^N (E_i - \bar{E})^2 \sum_{i=1}^N (P_i - \bar{P})^2}} \quad (14)$$

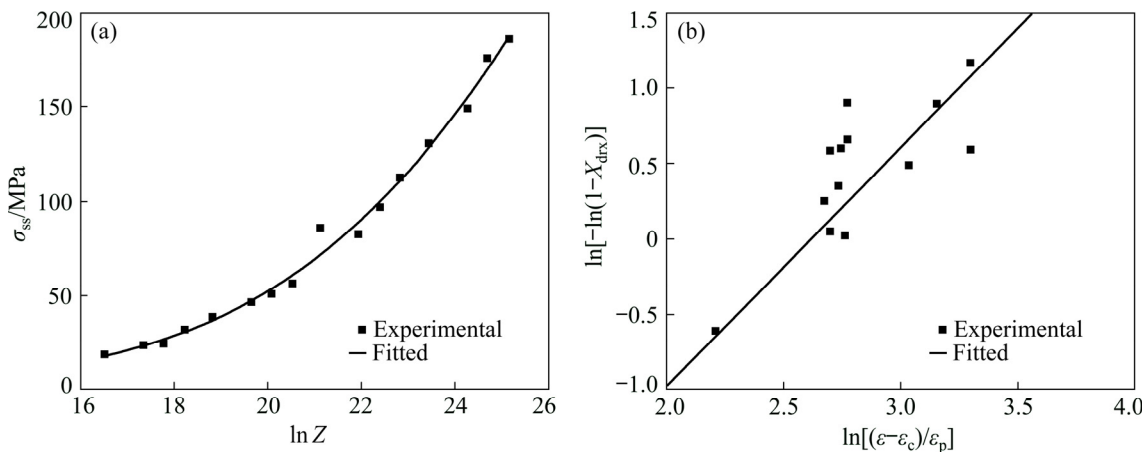


Fig. 10 Relationship between σ_{ss} and $\ln Z$ (a) and $\ln[-\ln(1-X_{\text{drx}})]$ and $\ln[(\varepsilon - \varepsilon_c)/\varepsilon_p]$ (b)

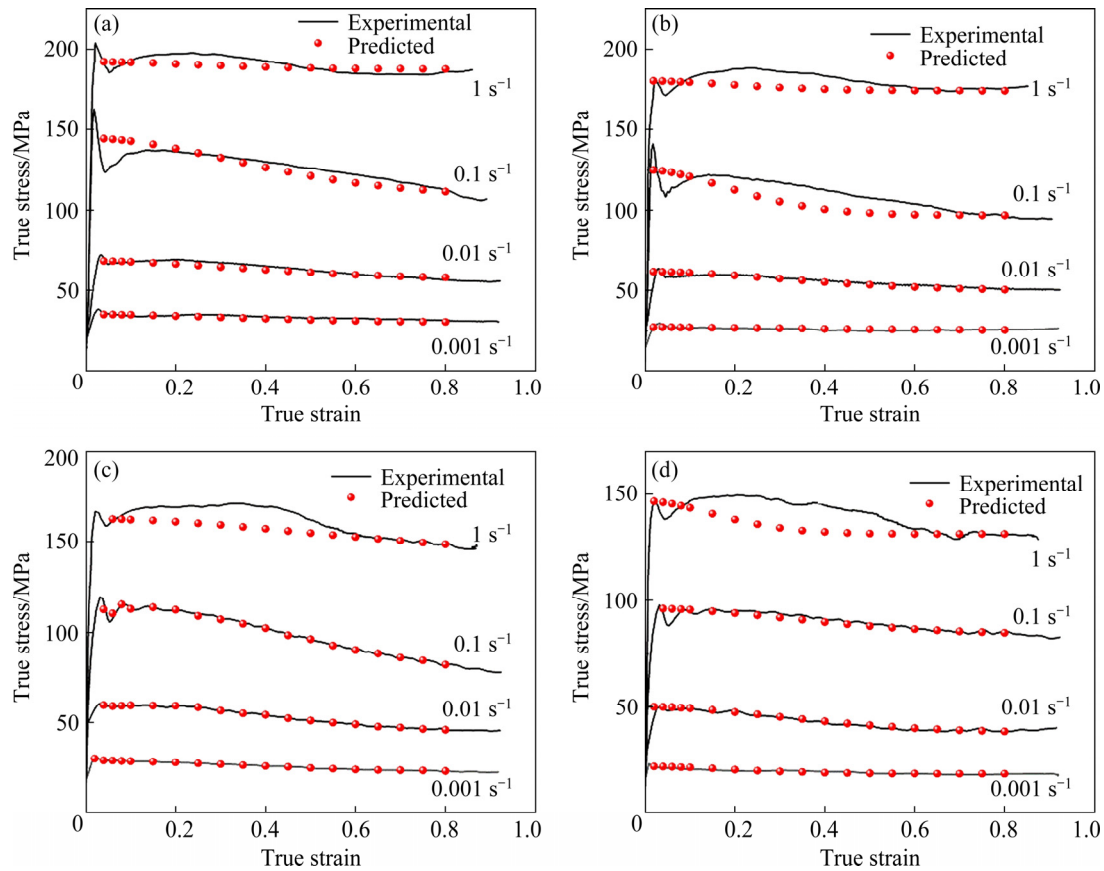


Fig. 11 Comparison between predicted values and experimental data at 820 °C (a), 840 °C (b), 860 °C (c), and 900 °C (d)

$$\text{AARE} = \frac{1}{N} \sum_{i=1}^N \left| \frac{E_i - P_i}{E_i} \right| \times 100\% \quad (15)$$

where E_i is the experimental data, P_i represents predicted value, \bar{E} and \bar{P} represent the average values of E_i and P_i , respectively, and N is the number of tests. The \bar{R} and AARE are both between 0 and 1 (100%). When the \bar{R} is close to 1, it means that the correlation between the experimental value and the predicted value is better. When the AARE is close to 0, it means that the relative error between the experimental value and the predicted value is small, and the accuracy of the constitutive model is high.

Figure 12 shows the correlation between the predicted stress and experimental stress, when the predicted value is close to the experimental value, the black data point is close to the red best correlation. The \bar{R} and AARE can be acquired from Fig. 12, which are 0.9919 and 3.331%, showing that high-temperature rheological behaviors of Ti-35421 alloys can be described by this model with high accuracy.

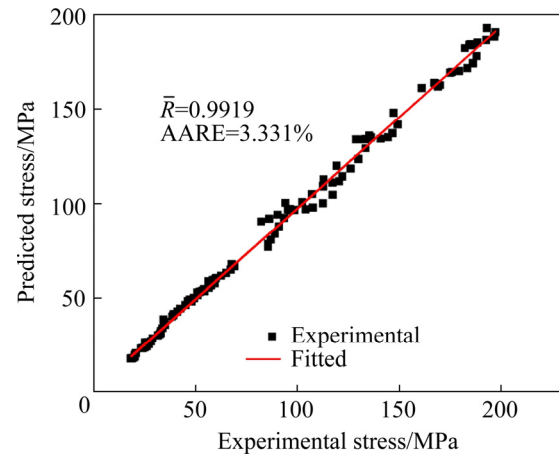


Fig. 12 Correlation between predicted stress and experimental stress

4 Discussion

4.1 Effects of WH, DRV and DRX on flow stress

During WH and DRV, the evolution of dislocation density with strain is mainly determined by two parts: multiplication and annihilation of dislocation. No significant softening stage appears during DRV-dominated hot deformation. When WH

caused by deformation and the softening caused by DRV are balanced, the flow stress no longer increases and the stress–strain curve remains horizontal. Figure 13(a) shows the comparison of experimental data and uncorrected data at 820 °C (Uncorrected data means that only the influence of WH and DRV on the flow stress is considered). The occurrence of DYP leads to that flow stress increases sharply and reaches its peak, and then it drops. Excluding the influence of the stress caused by DYP, it can be seen from Fig. 13(a) that experimental data and uncorrected data are in good agreement in WH and DRV stage ($\varepsilon < \varepsilon_c$). However, obvious softening phenomenon from the uncorrected data does not appear as the strain increases, and the reason is considered to be without the effect of the DRX. When DRX occurs, the flow stress gradually increases to the peak value and the softening effect of DRX is very obvious. The stress will gradually decrease and reach the steady-state stress finally.

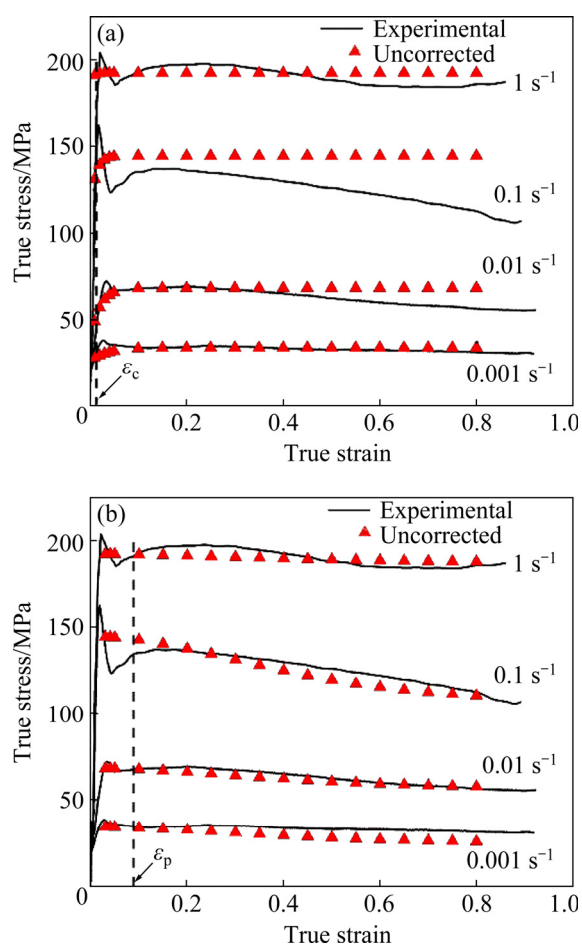


Fig. 13 Comparison of experimental data and uncorrected data at 820 °C: (a) Uncorrected data representing effects of WH and DRV; (b) Uncorrected data representing effect of DRX

Therefore, if only the effect of DRX on the stress–strain curve is considered, when the strain reaches the critical strain, the stress will gradually decrease to a steady state. Figure 13(b) shows the comparison of experimental data and uncorrected data at 820 °C (Uncorrected data mean that only the influence of DRX on flow stress is considered). It can be seen from Fig. 13(b) that when the $\varepsilon > \varepsilon_p$, experimental data and uncorrected data are in good agreement. However, when the $\varepsilon < \varepsilon_p$, the stress does not increase significantly as the strain increases. Large deviation between the experimental data and the uncorrected data is considered that the effects of WH and DRV are not taken into account here.

4.2 DRX mechanism

It can be seen from Fig. 4(m) that there are some LAGBs (white lines) inside the β grains. The original grains are divided into subgrains with different shapes and sizes. The color of some subgrains is consistent with the original grains, which means that the subgrains are separated from the original grains. Therefore, recrystallized grains are formed mainly through subgrain rotation at low strain rate (0.001 s^{-1}) and the DRX mechanism is CDRX. Line A in Fig. 4(c) and Line B in Fig. 4(o) were chosen to analyze misorientation distribution. The point-to-origin misorientation can be able to measure the misorientation from the reference point to a certain distance point. Figure 14 shows that the misorientation increases suddenly from the inside of the grain to the boundaries at the strain rate of 1 s^{-1} . However, when the strain rate is 0.001 s^{-1} , the increment is much less. This reveals that the DRV followed by CDRX by the progressive lattice rotation is the predominant mechanism [30]. Based on the facts above described, the predominant hot deformation mechanism of Ti-35421 alloy above T_β is concluded to be the progressive lattice rotation DRX followed by CDRX, and the deformation softening is controlled by DRV and DRX.

The accumulated misorientation increases from the interior of grain to the grain boundary gradually. The increment is more obvious when the strain rate increases, as shown in Fig. 14. The process may accelerate DRV near the grain boundary. Combined with the fact that some small recrystallized grains are formed near previously existing grain boundary, it is indicated that, besides the DRV, CDRX took place by the progressive

lattice rotation [38]. Figure 15 shows the kernel average misorientation (KAM) maps at 860 °C and different strain rates (0.001 s^{-1} and 1 s^{-1}). High KAM value at grain boundaries and low KAM value in grain interior are observed. The KAM maps can characterize the non-uniform distribution and defect density. A higher value indicates greater plastic deformation or a higher defect density. As we all know, KAM is the average misorientation of a determined point with its nearest neighbors. The

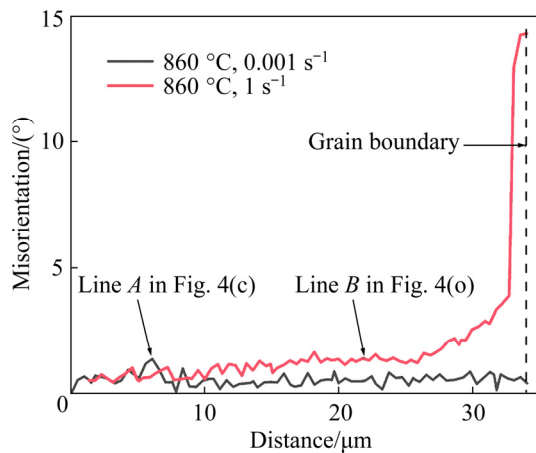


Fig. 14 Misorientation measured from grain interior to boundary after deformation at 860 °C with strain rates of 0.001 and 1 s^{-1}

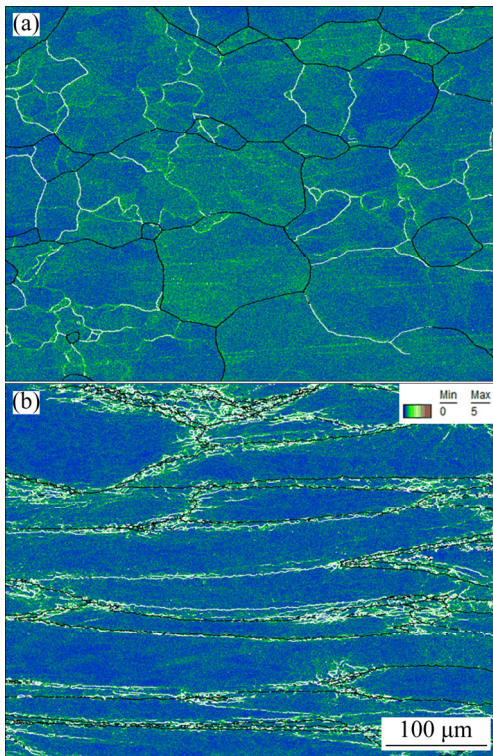


Fig. 15 KAM maps of Ti-35421 deformed at 860 °C and different strain rates: (a) 0.001 s^{-1} ; (b) 1 s^{-1}

high KAM density near the grain boundaries shows the increment of misorientation toward grain boundaries. Hence, the high KAM value near the previously existing grain boundary and the low KAM value in the interior of the grain indicate that CDRX occurs after DRV. This viewpoint has been proposed and verified in Ti-55531 alloy [38].

Figure 16 shows the orientation maps of Ti-35421 alloy at 900 °C and 1 s^{-1} with different height reductions. It can be seen from Fig. 16(a) that there are no LAGBs at the grain boundary before deformation. When the height reduction is 20%, some LAGBs appear at the grain boundaries (Fig. 16(b)). When the height reduction increases to 40%, more and more LAGBs are formed at the grain boundaries. The absorption dislocation of LAGBs gradually evolves into HAGBs, then a small number of recrystallized grains are formed near the grain boundaries (Fig. 16(c)). As the deformation continues, more and more LAGBs are transformed into HAGBs, and the number of recrystallized grains gradually increases (Fig. 16(d)).

Schematic diagrams of DRX for Ti-35421 alloy during hot deformation in the β single-phase region are illustrated in Fig. 17 [39]. The β grains in the initial structure are all equiaxed, as shown in Fig. 17(a). As the hot deformation perpendicular to the compression axis continues, the equiaxed grains are elongated (Figs. 17(b) and (c)). As the hot compression continues, the movement of dislocations and the migration of grain boundary will occur at this stage, which causes the grain boundary to become jagged (Fig. 17(c)). In order to reduce the stress concentration caused by dislocation movement, dislocations interact and form the subgrain boundaries. The subgrain boundaries increase the angle by absorbing dislocations. Eventually, the LAGBs change to the HAGBs boundaries, and the subgrains become the recrystallized grains (Figs. 17(d) and (e)).

The discontinuous dynamic recrystallization (DDRX) often occurs during hot deformation of materials with low and medium stacking fault energies. The typical feature of DDRX is the formation and growth of recrystallization nuclei through the migration of HAGBs. The percentage of HAGBs is related to the occurrence of DDRX. Generally, the proportion of HAGBs increases significantly when DDRX occurs. Figure 18 shows that the proportion of HAGBs does not increase

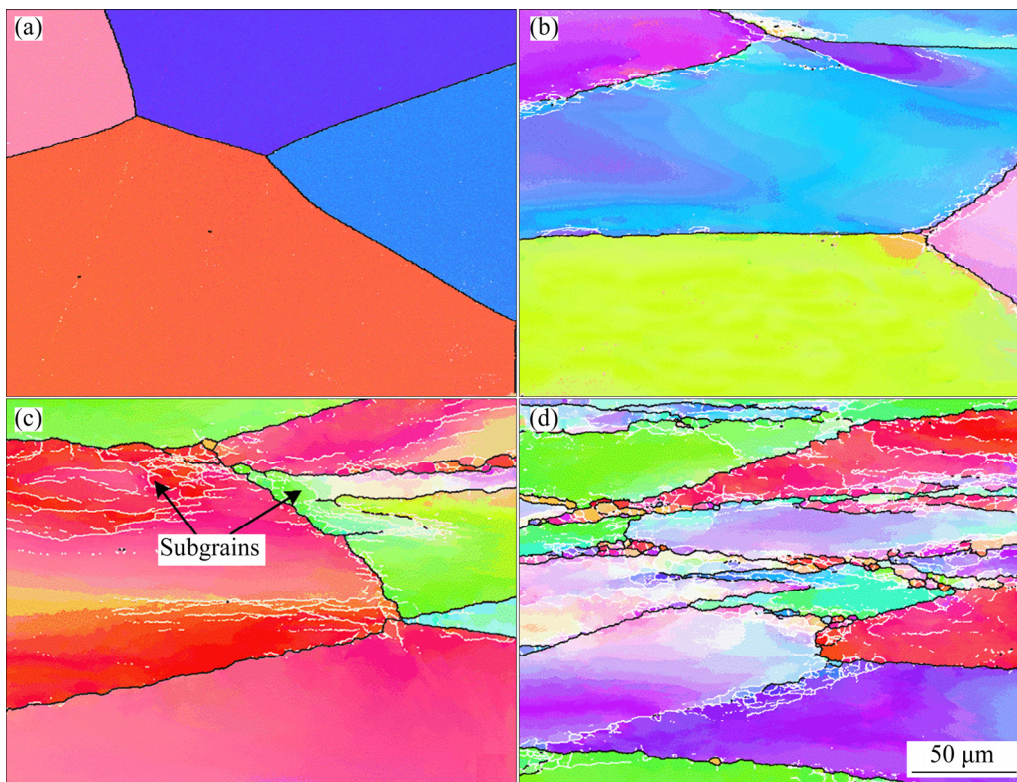


Fig. 16 Orientation maps of Ti-35421 alloy at 900 °C and 1 s^{-1} with different height reductions: (a) 0%; (b) 20%; (c) 40%; (d) 60%

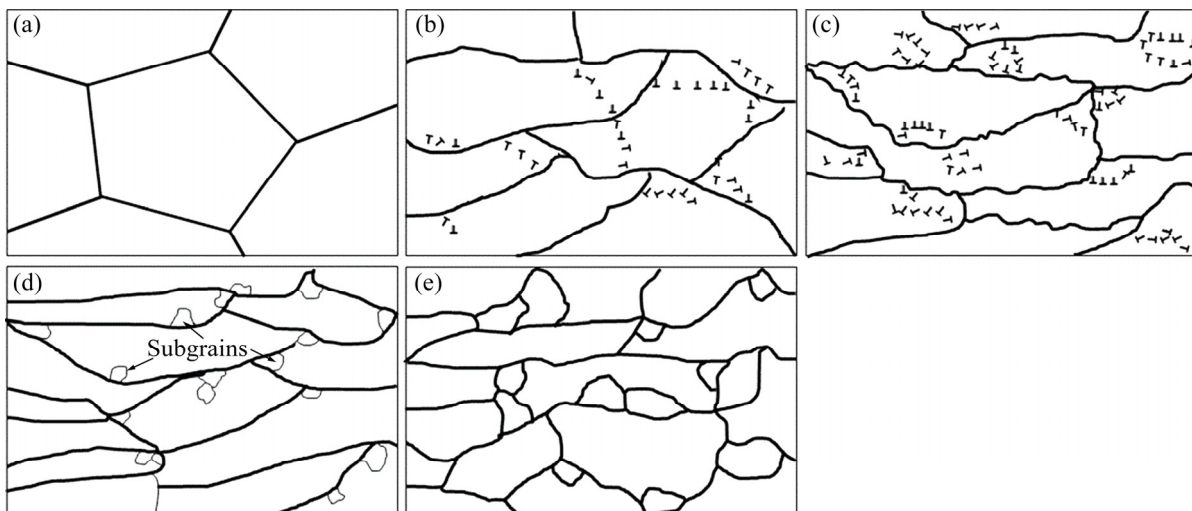


Fig. 17 Schematic diagrams of DRX for Ti-35421 alloy in β single-phase region [39]

with increasing temperature, indicating that no DDRX occurs. In addition, it can be known that the percentage of the HAGBs maintains a relatively constant value in CDRX, also showing that CDRX occurs instead of DDRX [40]. It can be seen from Fig. 18 that the proportions of HAGBs are higher at lower strain rates (45%–50% at 0.001 s^{-1} and 30%–35% at 0.1 s^{-1}). As the strain rate increases, due to the short deformation time, the dislocations

generated inside the deformed grains do not have enough time to migrate and form HAGBs, resulting in a low proportion.

4.3 Predicted size of recrystallized grains

4.3.1 Identification of recrystallized grains

Based on EBSD data of Ti-35421 alloys after the hot deformation, the microstructure evolution can be partitioned into the non-recrystallized and

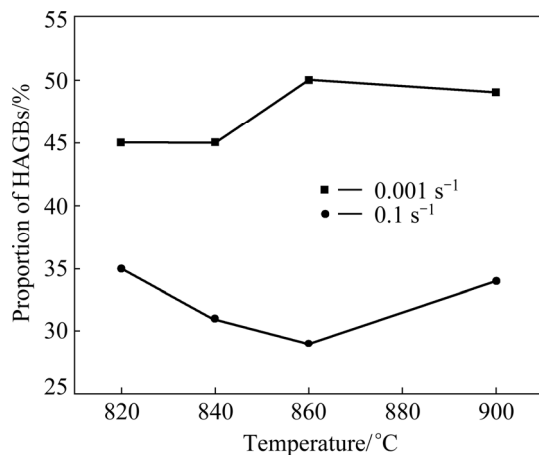


Fig. 18 Relationship between proportion of HAGBs and temperature

recrystallized sections using internal misorientation. This is a significant feature of deformed and recrystallized grains. The internal misorientation of the grain is related to the distortion mode and stored energy [41]. And it can be described by the grain orientation spread (GOS). The GOS value is related to dislocation content and stored energy, and higher GOS value represents higher dislocation content and stored energy. The recrystallized grains have lower dislocation content and the GOS value of recrystallized samples is lower. Therefore, the difference of GOS can be used to distinguish

the recrystallized and deformed grains. In general, a fixed GOS value is set to distinguish recrystallized and non-recrystallized grains [41]. The GOS value of dynamically recrystallized grains is between 1° and 2° [42]. In this study, the value of critical GOS is set to be 2° in order to distinguish the recrystallized grains and non-recrystallized grains. Figure 19 shows the division of recrystallized grains at 820°C and different strain rates. We can conclude that the GOS value can distinguish the recrystallized grains well and the recrystallized grains are formed at the grain boundaries. Figure 20 indicates the influence of deformation temperature and strain rate on volume fractions of recrystallized grains. At the high strain rates (1 s^{-1}), only a few small recrystallized grains are distributed at grain boundaries with the volume fraction of less than 10%. As the strain rate decreases, the volume fraction of recrystallized grains gradually increases, showing the gradual growth of recrystallized grains. There are two main reasons that can explain this phenomenon. One is that as the strain rate decreases, the critical strain required for dynamic recrystallization gradually decreases, and DRX can occur under smaller strain conditions. The other is that at a low strain rate, DRX has sufficient time to complete the growth process, which causes the volume fraction of the recrystallized grains to

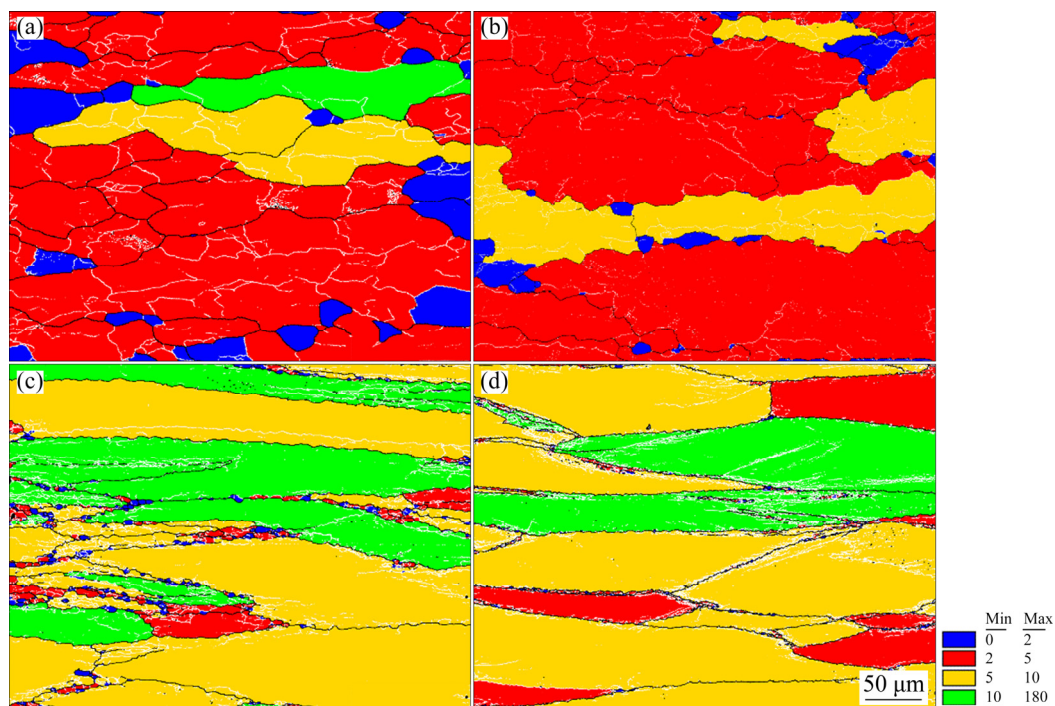


Fig. 19 Identification of recrystallized grains during hot deformation of Ti-35421 alloy: (a) 820°C , 0.001 s^{-1} ; (b) 820°C , 0.01 s^{-1} ; (c) 820°C , 0.1 s^{-1} ; (d) 820°C , 1 s^{-1}

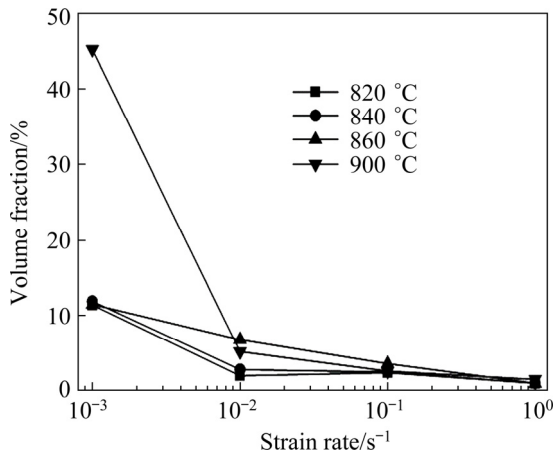


Fig. 20 Influence of deformation temperature and strain rate on volume fraction of recrystallized grains

gradually increase. Moreover, similar phenomenon occurs under different temperature conditions. There is also an increase tendency accompanying with the increase of the volume fraction of recrystallized grains at higher temperatures. This phenomenon can be ascribed to the higher migration rates of the grain boundaries and faster meeting of the demands of the activation energy for DRX process at higher deformation temperatures.

4.3.2 Comparison of predicted values with experimental data

The calculation of the grain size of recrystallized grains can be expressed as follows [33]:

$$d_{\text{drx}} = AZ^\beta \tag{16}$$

where d_{drx} is the average diameter of the recrystallized grains, and A and β are material constants.

Recrystallized grains can be distinguished by fixed GOS value and the average diameter of recrystallized grains can be calculated by OIM Analysis software. The calculation method is to sum the equivalent diameters of each grain together and then divide by the total number of grains. Five pictures are selected under each hot deformation condition to reduce errors. The relationship between $\ln d_{\text{drx}}$ and $\ln Z$ is depicted in Fig. 21. The values of A and β can be obtained by the intercept and slope of the fitted curve in Fig. 21 and are 37200 and -0.384 , respectively. Therefore, the fitted Zener–Hollomon function is formulated in Eq. (17) as follows:

$$d_{\text{drx}} = 37200Z^{-0.384} \tag{17}$$

The comparison of experimental data with simulated data of the average grain size of recrystallized grains under different hot deformation conditions are shown in Fig. 22. The deviations between the simulated results and the experimental

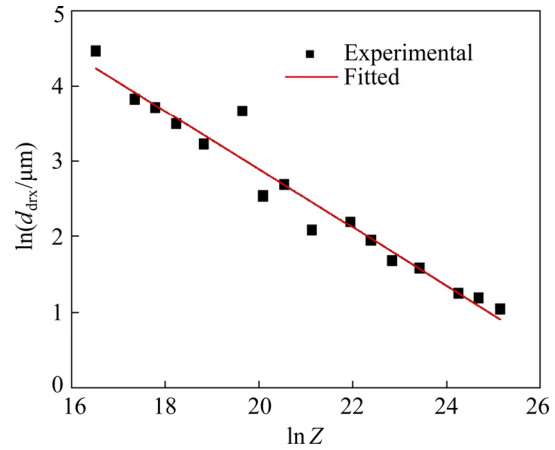


Fig. 21 Relationship between $\ln d_{\text{drx}}$ and $\ln Z$

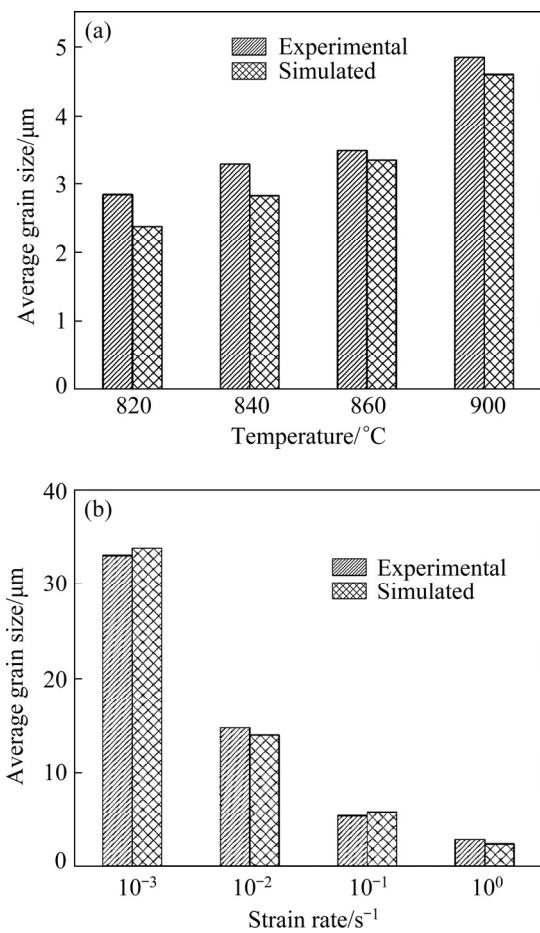


Fig. 22 Comparison between simulated and experimental data of average grain size of recrystallized grains under different hot deformation conditions: (a) At 1 s⁻¹ and different temperatures; (b) At 820 °C and different strain rates

results in Figs. 22(a) and (b) are 6.2% and 6.5%, respectively, which demonstrates that the simulated and experimental data are in good agreement. The increase of the recrystallized grain size with the increase in temperature in Fig. 22(a) is considered to be resulted from the fast boundary migration and high growth of the grains at high temperatures. Figure 22(b) shows that the grain size gradually decreases as the strain rate increases. The reason for this phenomenon is that there is not enough time for the grain growth at high strain rates. Experimental data of the corresponding grain size are shown in Fig. 19. At low strain rate (0.001 s^{-1}), the recrystallized grains and β grains merge with each other and grow up, and the average grain size of recrystallized grains is larger. However, when the strain rate is set to be 0.1 s^{-1} , the original grains are elongated and squashed. And only a few small recrystallized grains appear near the original grain boundaries, as shown in Fig. 19(c). The results show that calculation model of recrystallized grain size can accurately predict the change of recrystallized grain size of the Ti-35421 alloy during hot deformation.

5 Conclusions

(1) The discontinuous yield phenomenon and rheological softening of Ti-35421 alloys were observed on the stress–strain curves, and they are sensitive to the strain rates and deformation temperatures. The values of yield drop were related to thermal and decrease with decreasing temperature.

(2) The critical condition and kinetic model of Ti-35421 alloy were determined and the Arrhenius constitutive model were established. High temperature rheological behaviors of Ti-35421 alloys could be described by the equation with high accuracy.

(3) DRX occurred during hot deformation and the critical strain for DRX was determined. The volume fraction and grain size of recrystallized grains increased significantly with decreasing strain rate and increasing temperature. The prediction formula for the recrystallized grains during the hot deformation above T_β was established based on the newly developed Arrhenius constitutive model and microstructural changes. Good linear dependency

between the experimental value and the simulated value indicates that the present model can be used for the microstructural prediction with high accuracy.

(4) The deformation softening mechanism was controlled by DRV and DRX. The CDRX was observed and characterized through subgrain rotation. The sudden increase of misorientation from the inside of the grain to the boundaries at different strain rates reveals that the DRV followed by CDRX by progressive lattice rotation is the predominant mechanism.

Acknowledgments

The authors are grateful for the financial supports from the National Natural Science Foundation of China (Nos. 52001163, 52075237), and the Primary Research and Development Plan of Jiangsu Province, China (No. BE2019119).

References

- [1] RAO K T V, KIM Y W, RITCHIE R O. High-temperature fatigue-crack growth behavior in a two-phase ($\gamma+\alpha_2$) TiAl intermetallic alloy [J]. *Scripta Metallurgica et Materialia*, 1995, 33: 459–465.
- [2] NIINOMI M. Recent research and development in titanium alloys for biomedical applications and healthcare goods [J]. *Science and Technology of Advanced Materials*, 2003, 4: 445–454.
- [3] TAN K, LI J, GUAN Z J, YANG J B, SHU J X. The identification of dynamic recrystallization and constitutive modeling during hot deformation of Ti55511 titanium alloy [J]. *Materials & Design*, 2015, 84: 204–211.
- [4] RAGHUNATHAN S L, STAPLETON A M, DASHWOOD R J, JACKSON M, DYE D. Micromechanics of Ti–10V–2Fe–3Al: In situ synchrotron characterisation and modelling [J]. *Acta Materialia*, 2007, 55: 6861–6872.
- [5] BOYER R R, BRIGGS R D. The use of β titanium alloys in the aerospace industry [J]. *Journal of Materials Engineering and Performance*, 2013, 22: 2916–2920.
- [6] JACKSON M, DASHWOOD R, FLOWER H, CHRISTODOULOU L. The microstructural evolution of near beta alloy Ti–10V–2Fe–3Al during subtransus forging [J]. *Metallurgical and Materials Transactions A*, 2005, 36: 1317–1327.
- [7] PETERS M, HEMPTENMACHER J, KUMPFERT J, LEYENS C. Titan und titanlegierungen: Struktur, gefüge, eigenschaften [M]. Koln: Wiley-VCH, 2002: 139–161. (in German)
- [8] LI Y H Z, OU X Q, NI S, SONG M. Deformation behaviors of a hot rolled near- β Ti–5Al–5Mo–5V–1Cr–1Fe alloy [J]. *Materials Science and Engineering A*, 2019, 742: 390–399.
- [9] WU C, HUANG L, LI C M. Experimental investigation on dynamic phase transformation and texture evolution of

- Ti55531 high strength titanium alloy during hot compression in the $\alpha+\beta$ region [J]. *Materials Science and Engineering A*, 2020, 773: 138851.
- [10] HUA K, XUE X Y, KOU H C, FAN J K, TANG B, LI J S. Characterization of hot deformation microstructure of a near beta titanium alloy Ti-5553 [J]. *Journal of Alloys and Compounds*, 2014, 615: 531–537.
- [11] LEI L M, HUANG X, WANG M M, WANG L Q, QIN J N, LI H P, LU S Q. Effect of hot compressive deformation on the martensite transformation of Ti-10V-2Fe-3Al titanium alloy [J]. *Materials Science and Engineering A*, 2011, 530: 591–601.
- [12] CHANG H, ZENG W D, LUO Y Y, ZHOU Y G, ZHOU L. Phase transformation and microstructure evolution in near beta Ti-B19 titanium alloy during aging treatment [J]. *Rare Metal Materials and Engineering*, 2006, 35: 1589–1592.
- [13] LI D. A study on microstructure and mechanical properties of Ti-35421 alloy with high strength and toughness [D]. Nanjing: Nanjing Tech University, 2017: 45–46. (in Chinese)
- [14] WAN Z P, SUN Y, HU L X, YU H. Dynamic softening behavior and microstructural characterization of TiAl-based alloy during hot deformation [J]. *Materials Characterization*, 2017, 130: 25–32.
- [15] SUN Y, ZHANG H, WAN Z P, REN L L, HU L X. Establishment of a novel constitutive model considering dynamic recrystallization behavior of Ti-22Al-25Nb alloy during hot deformation [J]. *Transactions of Nonferrous Metals Society of China*, 2019, 29: 546–557.
- [16] QIN C, YAO Z K, NING Y Q, SHI Z F, GUO H Z. Hot deformation behavior of TC11/Ti-22Al-25Nb dual-alloy in isothermal compression [J]. *Transactions of Nonferrous Metals Society of China*, 2015, 25: 2195–2205.
- [17] ZHAO H J, WANG B Y, JU D Y, CHEN G J. Hot tensile deformation behavior and globularization mechanism of bimodal microstructured Ti-6Al-2Zr-1Mo-1V alloy [J]. *Transactions of Nonferrous Metals Society of China*, 2018, 28: 2449–2459.
- [18] LIU G F, ZHANG S Z, CHEN L Q. Hot deformation behavior of Ti-6.5Al-3.5Mo-1.5Zr-0.3Si alloy with acicular microstructure [J]. *Journal of Central South University of Technology*, 2011, 18: 296–302.
- [19] URCOLA J J, SELLARS C M. Influence of changing strain rate on microstructure during hot deformation [J]. *Acta Metallurgica*, 1987, 35: 2649–2657.
- [20] ZENG Z P, JONSSON S, ROVEN H J. The effects of deformation conditions on microstructure and texture of commercially pure Ti [J]. *Acta Materialia*, 2009, 57(19): 5822–5833.
- [21] LIANG H Q, GUO H Z, NING Y Q, PENG X N, QIN C, SHI Z F, NAN Y. Dynamic recrystallization behavior of Ti-5Al-5Mo-5V-1Cr-1Fe alloy [J]. *Materials & Design*, 2014, 63: 798–804.
- [22] BALASUBRAHMANYAM V V, PRASAD Y V R K. Deformation behaviour of beta titanium alloy Ti-10V-4.5Fe-1.5Al in hot upset forging [J]. *Materials Science and Engineering A*, 2002, 336: 150–158.
- [23] WANG Q W, LIN Y C, JIANG Y Q, LIU X G, ZHANG X Y, CHEN D D, CHEN C, ZHOU K C. Precipitation behavior of a β -quenched Ti-5Al-5Mo-5V-1Cr-1Fe alloy during high-temperature compression [J]. *Materials Characterization*, 2019, 151: 358–367.
- [24] LIU B, LIU Y, LI Y P, ZHANG W, CHIBA A. Thermomechanical characterization of β -stabilized Ti-45Al-7Nb-0.4W-0.15B alloy [J]. *Intermetallics*, 2011, 19: 1184–1190.
- [25] ZHAO J, ZHONG J, YAN F, CHAI F, DARGUSCH M. Deformation behaviour and mechanisms during hot compression at supertransus temperatures in Ti-10V-2Fe-3Al [J]. *Journal of Alloys and Compounds*, 2017, 710: 616–627.
- [26] WEISS I, SEMIATIN S L. Thermomechanical processing of beta titanium alloys—An overview [J]. *Materials Science and Engineering A*, 1998, 243: 46–65.
- [27] PHILIPPART I, RACK H J. High temperature dynamic yielding in metastable Ti-6.8Mo-4.5F-1.5Al [J]. *Materials Science and Engineering A*, 1998, 243: 196–200.
- [28] FAN X G, ZHANG Y, GAO P F, LEI Z N, ZHAN M. Deformation behavior and microstructure evolution during hot working of a coarse-grained Ti-5Al-5Mo-5V-3Cr-1Zr titanium alloy in beta phase field [J]. *Materials Science and Engineering A*, 2017, 694: 24–32.
- [29] FAN J K, KOU H C, LAI M J, TANG B, CHANG H, LI J S. High temperature discontinuous yielding in a new near- β titanium alloy Ti-7333 [J]. *Rare Metal Materials and Engineering*, 2014, 43: 808–812.
- [30] WARCHOMICKA F, POLETTI C, STOCKINGER M. Study of the hot deformation behaviour in Ti-5Al-5Mo-5V-3Cr-1Zr [J]. *Materials Science and Engineering A*, 2011, 528: 8277–8285.
- [31] ZENER C, HOLLOMON J H. Effect of strain rate upon plastic flow of steel [J]. *Journal of Applied Physics*, 1944, 15: 22–32.
- [32] SELLARS C M, MCTEGART W J. On the mechanism of hot deformation [J]. *Acta Metallurgica*, 1966, 14: 1136–1138.
- [33] WU C, HUANG L. Hot deformation and dynamic recrystallization of a near-beta titanium alloy in the β single phase region [J]. *Vacuum*, 2018, 156: 384–401.
- [34] GOTTSSTEIN G, FROMMERT M, GOERDELER M, SCHAFER N. Prediction of the critical conditions for dynamic recrystallization in the austenitic steel 800H [J]. *Materials Science and Engineering A*, 2004, 387: 604–608.
- [35] POLIAK E I, JONAS J J. A one-parameter approach to determining the critical conditions for the initiation of dynamic recrystallization [J]. *Acta Materialia*, 1996, 44: 127–136.
- [36] PRASAD Y V R K, RAO K P. Processing maps for hot deformation of rolled AZ31 magnesium alloy plate: Anisotropy of hot workability [J]. *Materials Science and Engineering A*, 2008, 487: 316–327.
- [37] XIA Y F, JIANG W, CHENG Q, JIANG L, JIN L. Hot deformation behavior of Ti-6Al-4V-0.1Ru alloy during isothermal compression [J]. *Transactions of Nonferrous Metals Society of China*, 2020, 30: 134–146.
- [38] DIKOVITS M, POLETTI C, WARCHOMICKA F. Deformation mechanisms in the near- β titanium alloy Ti-55531 [J]. *Metallurgical and Materials Transactions A*, 2014, 45: 1586–1596.

- [39] FAN J K, KOU H C, LAI M J, TANG B, CHANG H, LI J S. Hot deformation mechanism and micro-structure evolution of a new near β titanium alloy [J]. Materials Science and Engineering A, 2013, 584: 121–132.
- [40] JAZAERI H, HUMPHREYS F J. The transition from discontinuous to continuous recrystallization in some aluminium alloys. II: Annealing behaviour [J]. Acta Materialia, 2004, 52: 3251–3262.
- [41] GAZDER A A, SÁNCHEZ-ARAIZA M, JONAS J J, PERELOMA E V. Evolution of recrystallization texture in a 0.78 wt.% Cr extra-low-carbon steel after warm and cold rolling [J]. Acta Materialia, 2011, 59: 4847–4865.
- [42] BARRETT C D, IMANDOUST A, OPPEL A L, INAL K, TSCHOPP M A, EL KADIRI H. Effect of grain boundaries on texture formation during dynamic recrystallization of magnesium alloys [J]. Acta Materialia, 2017, 128: 270–283.

Ti-35421 合金在 β 单相区的热变形行为及动态再结晶机制

路通^{1,2}, 淡振华¹, 李凯³, 易丹青⁴, 周廉¹, 常辉¹

1. 南京工业大学 材料科学与工程学院 先进材料技术研究所, 南京 210009;

2. 中铝材料应用研究院有限公司 苏州分公司, 苏州 215026;

3. 中铝材料应用研究院有限公司, 北京 102209;

4. 中南大学 材料科学与工程学院, 长沙 410083

摘要: 利用 Gleeble-3500 热模拟试验机对 Ti-3Al-5Mo-4Cr-2Zr-1Fe (Ti-35421)合金进行 β 单相区等温压缩实验, 研究该合金在变形温度为 820~900 °C、应变速率为 0.001~1 s⁻¹ 的热变形行为和显微组织演化。研究结果表明, 该合金的不连续屈服现象和流变软化受应变速率和变形温度的影响。确定 Ti-35421 合金的动态再结晶临界条件和动力学模型, 并建立 Arrhenius 本构模型, 该本构模型可准确预测 Ti-35421 合金在 β 相转变温度以上的流变行为。EBSD 结果证明, 变形软化机制为动态回复和动态再结晶。此外, 确定热变形中的再结晶机制为连续动态再结晶, 并建立再结晶晶粒尺寸的计算模型。通过对比发现, 再结晶晶粒尺寸的实验值和预测值间具有良好的线性相关性, 表明该模型可精确预测再结晶晶粒尺寸的变化。

关键词: Ti-3Al-5Mo-4Cr-2Zr-1Fe 合金; 显微组织演化; Arrhenius 本构模型; 变形软化; 连续动态再结晶

(Edited by Wei-ping CHEN)